



Promotional role of B₂O₃ in enhancing hollow SnO₂ anode performance for Li-ion batteries



Ruiqing Liu^a, Deyu Li^a, Dong Tian^a, Guofeng Xia^a, Chen Wang^a, Ning Xiao^a, Ning Li^{a,*}, Nathan H. Mack^b, Qing Li^b, Gang Wu^{b,*}

^a School of Chemical Engineering & Technology, Harbin Institute of Technology, Harbin 150001, China

^b Materials Physics and Applications Division, Los Alamos National Laboratory, Los Alamos, NM 87545, USA

HIGHLIGHTS

- A core–shell structured hollow B₂O₃@SnO₂ anode was developed for LIBs.
- The new SnO₂-based composite anode exhibited much improved cyclic stability.
- A synergistic effect between B₂O₃ shells and hollow SnO₂ core is very likely.

ARTICLE INFO

Article history:

Received 8 September 2013

Received in revised form

11 November 2013

Accepted 21 November 2013

Available online 1 December 2013

Keywords:

SnO₂

B₂O₃

Core–shell structure

Composites

Anode

Lithium ion batteries

ABSTRACT

A composite anode consisting of hollow SnO₂ microspheres covered by glass-like B₂O₃ layers was prepared via a combined hydrothermal-impregnation method, which results in much improved electrochemical performance in lithium ion batteries, relative to pristine SnO₂ anodes. The cycling and rate capabilities of the SnO₂–B₂O₃ composite anodes were investigated as a function of B₂O₃ content. The balance between increased electron-acceptor effect and compromised electronic conductivity due to addition of B₂O₃ is maximized around 20 wt% B₂O₃ loading. The best performing SnO₂–B₂O₃ composite anode exhibits a specific capacity of 622.7 mAh g^{−1} up to 160 cycles, and is able to maintain a capacity above 528.6 mAh g^{−1} at rate of 5C. These enhanced performance characteristics are attributed to the unique composite structures consisting of the hollow SnO₂ cores and the B₂O₃ buffer layers, which likely are beneficial for reducing the overall volume changes. Importantly, the decreased charge transfer resistance and increased Li⁺ diffusion coefficient, resulting from B₂O₃ coating, lead to overall improvement of rate performance for the composite anodes. Such-fabricated composite structures are stable during the Li⁺ insertion/extraction, thereby promoting cycling stability.

© 2013 Elsevier B.V. All rights reserved.

1. Introduction

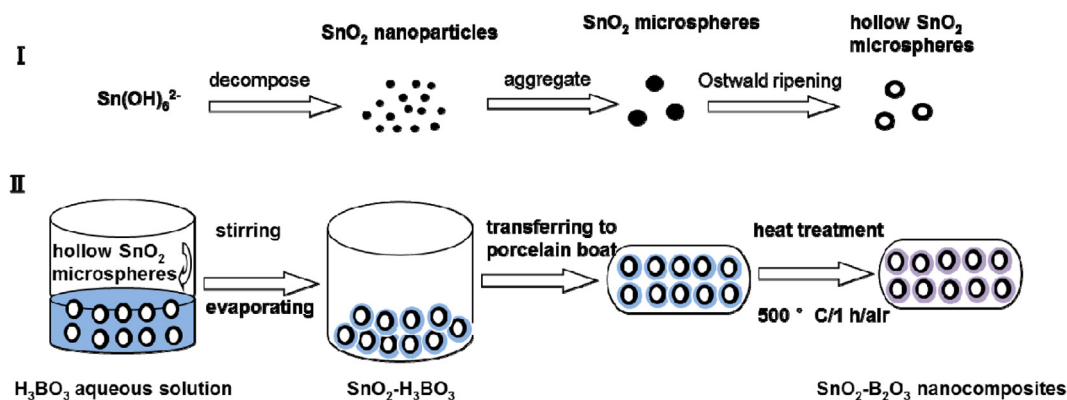
Tin dioxide (SnO₂) is a promising anode material for Li-ion batteries (LIBs) [1], because of its high theoretical specific capacity (780 mAh g^{−1}), as compared to currently used graphite materials (372 mAh g^{−1}) [2–6]. However, the pulverization of SnO₂ electrodes during the charge–discharge process leads to poor cycling performance [7]. Thus, its practical application as LIB anode has been significantly limited by the rapid capacity degradation. In order to mitigate this pulverization problem, various nanosized SnO₂ anodes were prepared to improve their cycling stability, due

to the reduced internal strain and shortened lithium diffusion length usually observed in nanostructured SnO₂ [8–10]. In particular, various synthetic approaches are able to alter the SnO₂ morphology with unique nanostructures, such as nanorod arrays [4], nanotubes [11], core–shell structures [12–14] and hollow nanostructures [5,15–17], showing enhanced structural stability by accommodating the volume change associated with Li insertion–extraction into vacancies in SnO₂ lattice. In addition, SnO₂ combining with buffer layers (e.g., graphene, conductive polymer) tends to increase the performance, due to their enhanced electronic conductivity and structural stability [18–23].

Alternatively, compared with carbon, boron atom may act as an electron-acceptor during the electron transfer process accompanied with lithium insertion due to its electron-deficient nature. Thus, more lithium species are reversibly inserted into the host matrix [24]. Our recent effort suggests that B₂O₃ is an effective

* Corresponding authors.

E-mail addresses: lininghit@263.net (N. Li), wugang@lanl.gov, wuglanl@gmail.com (G. Wu).



Scheme 1. Schematic illustration of the preparation of hollow $\text{SnO}_2\text{-B}_2\text{O}_3$ core-shell composites.

addition to enhance cycling stability of SnO_2 anode [25]. However, in that work, the SnO_2 in the composites are solid particles, where the internal strain is, thus, easy to be accumulated. Recently, hollow structure was found effective to reduce the overall volume changes and to provide increased interfacial areas for Li insertion–extraction [6]. Thus, there will still have more room to improve the electrochemical performances of SnO_2 anodes by simultaneously taking advantages of hollow structured and addition of B_2O_3 .

In this work, hollow SnO_2 microspheres were prepared and combined with a carbon-free buffer layer (B_2O_3) to develop a new $\text{SnO}_2\text{-B}_2\text{O}_3$ composite *via* a hydrothermal-impregnation method. The reduced charge transfer resistance and enhanced ionic conductivity were observed with the $\text{SnO}_2\text{-B}_2\text{O}_3$ composite anodes due to the presence of B_2O_3 . The correlation between electrochemical properties and B_2O_3 content was systematically studied with an aim to guide further materials design and synthesis.

2. Experimental section

2.1. Materials preparation

Hollow SnO_2 microspheres were prepared using a method as described in our previous work [5]. Briefly, $\text{CO}(\text{NH}_2)_2$ (1.922 g) and $\text{Na}_2\text{SnO}_3 \cdot 3\text{H}_2\text{O}$ (1.2802 g) were dissolved in 320 mL of water and ethanol ($\text{EtOH}/\text{H}_2\text{O} = 0.6$, V/V). This solution was transferred to a 400 mL Teflon-lined stainless steel autoclave at 180°C for 24 h. After cooling to room temperature, the white precipitation was collected by centrifugation and thoroughly washed followed by drying at 90°C for overnight. Then, hollow $\text{SnO}_2\text{-B}_2\text{O}_3$ core-shell nanocomposites were synthesized by impregnating the prepared hollow SnO_2 microspheres (0.4 g) with an aqueous solution containing varying H_3BO_3 content (0.0374 g, 0.0789 g, 0.1254 g, 0.1776 g, 0.2368 g). Keep stirring for 1.0 h and then evaporating to dry at 70°C . Finally, a heat treatment under air atmosphere was carried out at 500°C for 1.0 h. The detailed preparation procedure was depicted in Scheme 1. According to the B content in the composites, the prepared samples with different B_2O_3 contents were labeled as B 0.9%, B 1.1%, B 1.9%, B 2.1%, B 3.2%. A hollow SnO_2 control sample was prepared under identical conditions without adding H_3BO_3 precursor, labeled as B 0%.

2.2. Physical characterization

The samples were characterized with X-ray diffraction (XRD, Rigaku D/MAX-RB with $\text{Cu-K}\alpha$ radiation, $\lambda = 1.5418 \text{ \AA}$), field-emission Scanning electron microscopy (FE-SEM, Hitachi S4800 at 15 kV), Transmission electron microscopy (TEM, FEI TECNAI G2 at 200 kV), and X-ray photoelectron spectroscopy (XPS, VG K-Alpha).

2.3. Electrochemical measurements

Electrochemical tests were carried out at room temperature using lithium sheets as the combined counter and reference electrode. The working electrode consisted of 80 wt% active anode materials, 10 wt% acetylene black, and 10 wt% polyvinylidene fluoride (PVDF). 1.0 M LiPF_6 ethylenecarbonate (EC) and dimethyl carbonate (DMC) in a 1:1 volume ratio was used as the electrolyte. CR 2032 coin cells were used to assembly the electrodes in an argon-filled glove box with controlled moisture and oxygen concentrations below 1.0 ppm.

The assembled coin cells underwent galvanostatic charge–discharge cycling using a battery testing system (CT-3008W, NEWARE). The charge–discharge tests were conducted at the rate of 0.2 C ($1 \text{ C} = 780 \text{ mA g}^{-1}$) in the voltage window of 0.04–2.00 V (vs. Li/Li^+). The amount of SnO_2 was used to calculate the specific capacity of anode in LIBs. Cyclic voltammogram (CV) measurements were carried out using an electrochemical workstation CHI660B in a potential range of 0.02–2.70 V (vs. Li/Li^+) at a scan rate of 0.5 mV s^{-1} . Electrochemical impedance spectroscopy (EIS) was measured in a frequency range from 10^5 to 0.01 Hz with an AC amplitude of 5 mV. The real (Z') and imaginary (Z'') components of electrochemical impedance spectra in the Nyquist plot were analyzed using a complex nonlinear least squares (CNLS) fitting program to simulate equivalent resistances and capacitances.

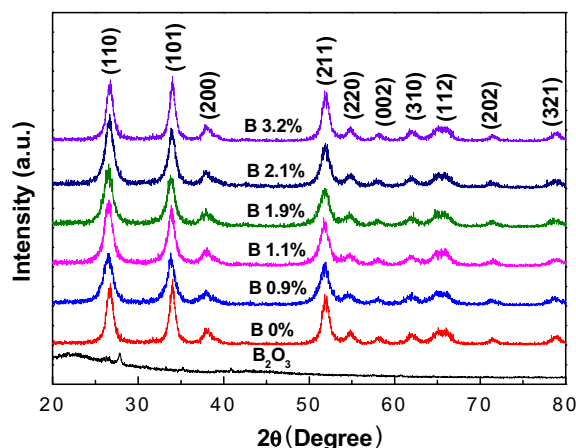


Fig. 1. XRD patterns for B_2O_3 and hollow $\text{SnO}_2\text{-B}_2\text{O}_3$ composites with different B_2O_3 content.

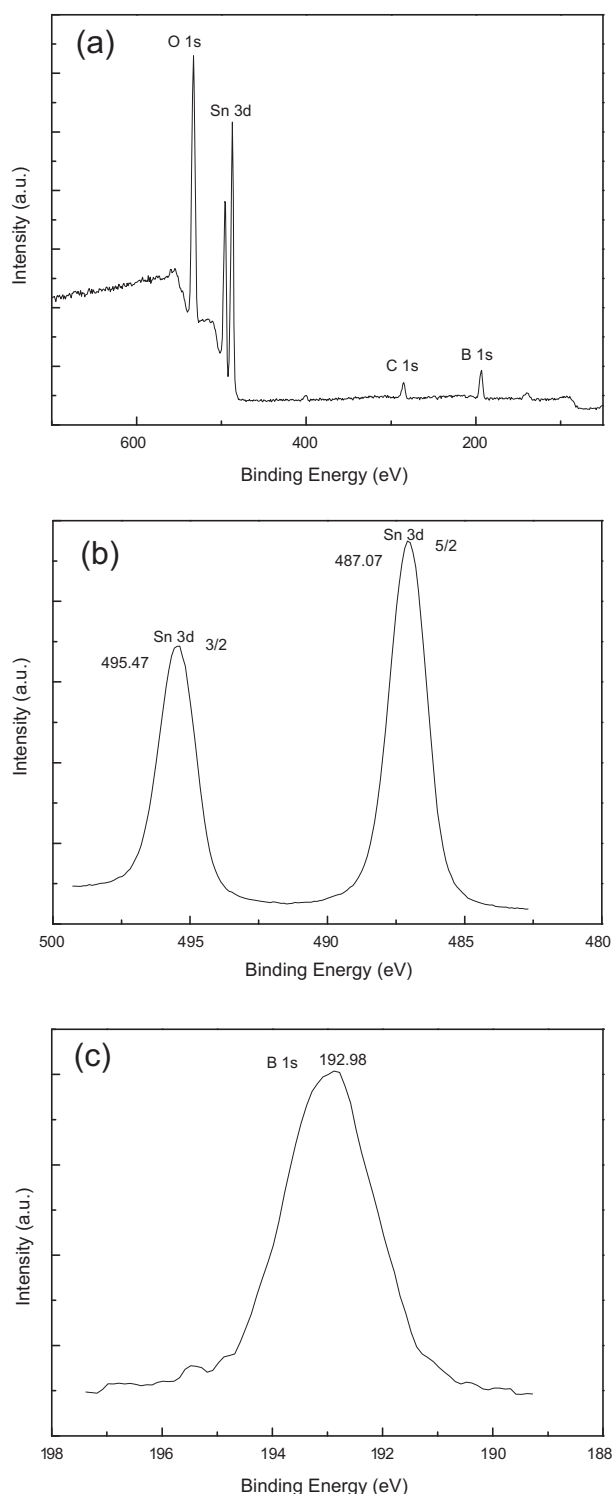


Fig. 2. XPS data for the hollow $\text{SnO}_2\text{--B}_2\text{O}_3$ core-shell composites (B 2.1%): (a) survey scan, (b) Sn 3d, and (c) B 1s spectra.

3. Results and discussion

3.1. Materials structure and morphology

Fig. 1 shows the XRD patterns for the $\text{SnO}_2\text{--B}_2\text{O}_3$ nano-composites and the individual B_2O_3 . As for the B_2O_3 sample, it was prepared by calcining H_3BO_3 at 500 °C for 1.0 h, which is under identical conditions for the preparation of $\text{SnO}_2\text{--B}_2\text{O}_3$ composites,

but without adding SnO_2 particles. There is no diffraction peak can be detected except for the broad peak around 22.5° and a small weak peak at 27.8° corresponding to amorphous B_2O_3 [26]. In addition, compared to the SnO_2 controls, the nearly identical XRD patterns of the $\text{SnO}_2\text{--B}_2\text{O}_3$ composites with various B_2O_3 content indicate that the amorphous phase B_2O_3 has little influence on SnO_2 crystal structures. As a result, all of the diffraction peaks can be well indexed to the tetragonal rutile structure of SnO_2 (cassiterite, JCPDS no. 41-1445). For instance, the identified diffraction peaks at 26.5° , 33.8° , 37.8° , 51.8° , 54.6° , 57.8° , 61.7° , 65.1° , 71.3° and 78.7° can be assigned to (110), (101), (200), (211), (220), (002), (310), (112), (202), and (321) planes of tetragonal SnO_2 [27–29]. No unknown peak was detected with the $\text{SnO}_2\text{--B}_2\text{O}_3$ composites, suggesting no any other crystalline borne phase formed during the synthesis.

As shown in Fig. 2, XPS measurements for the best performing $\text{SnO}_2\text{--B}_2\text{O}_3$ composite (B 21%) have been done to determine the oxidation state of Sn and B. Fig. 2a is the survey scan to identify the possible elements in the $\text{SnO}_2\text{--B}_2\text{O}_3$ composites, which includes Sn, B, O, and C. The C 1s peak observed in the spectra is due to the presence of conductive adhesive in the measurement. Further high-resolution spectra (Fig. 2b) confirms the presence of SnO_2 with the Sn 3d 3/2 and Sn 3d 5/2 locate at 495.5 eV and 487.1 eV, respectively. The binding energy of B 1s is 193.0 eV (Fig. 2c) that is similar to that of B 1s in B_2O_3 (193.0 eV [24], 193.1 eV [30]). Therefore, the existence of B is in the form of B_2O_3 .

The weight percentages of elements in different $\text{SnO}_2\text{--B}_2\text{O}_3$ composites determined by EDX are listed in Table 1. The calculated B_2O_3 contents in different $\text{SnO}_2\text{--B}_2\text{O}_3$ composites are 0, 6.64, 10.67, 14.55, 19.34, and 24.79 wt%. These $\text{SnO}_2\text{--B}_2\text{O}_3$ electrodes are accordingly labeled as B 0%, B 0.9%, B 1.1%, B 1.9%, B 2.1% and B 3.2% based on their boron content, which are used in the following text.

The morphology of the $\text{SnO}_2\text{--B}_2\text{O}_3$ samples was further examined by SEM and TEM images. As for the SEM images shown in Fig. 3a the diameter of SnO_2 microspheres (B 0%) is in the range of 200–500 nm. The $\text{SnO}_2\text{--B}_2\text{O}_3$ core-shell composites observed in (Fig. 3b–f) are in the range of 500–900 nm, indicating a larger size relative to the hollow SnO_2 microspheres. This increase in diameter is largely due to particle agglomeration during the impregnating and stirring steps during the synthesis. The representative TEM images for B 0% (no B_2O_3) and B 2.1% (around 20 wt% B_2O_3) are further compared in Fig. 4. It can be seen that typical hollow features with a brighter interior zone are surrounded by an outside dark ring at the edges of the particles, suggesting a shell thickness of approximately 30 nm. Furthermore, the crystal structures and edges of $\text{SnO}_2\text{--B}_2\text{O}_3$ (B 2.1%) were determined with HRTEM (Fig. 4d) showing clear lattice fringes (circle marked SnO_2 nanoparticles) and an interplanar spacing of about 0.335 nm corresponding to the (110) planes of SnO_2 . These data are in good agreement with the XRD results and indicate the formation of a highly crystallized rutile SnO_2 phase. Moreover, the amorphous B_2O_3 coating with a thickness of about 2–5 nm on the hollow sphere surface can be observed.

Table 1

Elemental qualification of $\text{SnO}_2\text{--B}_2\text{O}_3$ composites with different B_2O_3 content determined by EDS.

Samples	Sn (wt%)	O (wt%)	B (wt%)
B 0%	77.74	22.26	—
B 0.9%	89.51	9.62	0.87
B 1.1%	82.95	15.94	1.11
B 1.9%	77.01	21.10	1.89
B 2.1%	69.20	28.66	2.14
B 3.2%	60.82	35.97	3.21

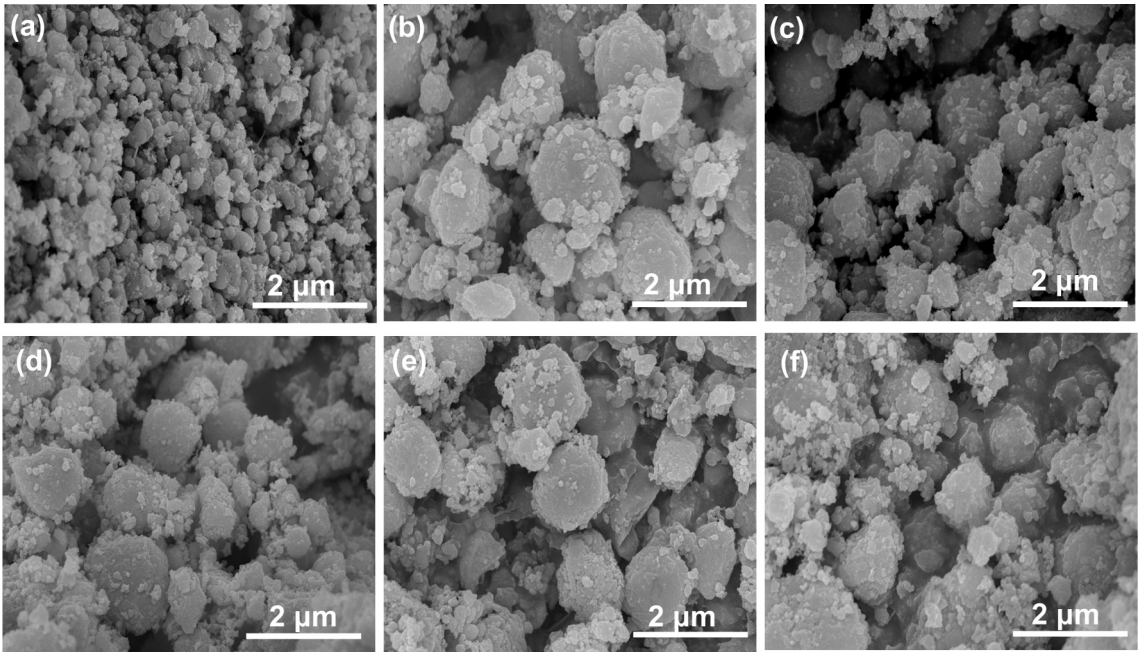


Fig. 3. SEM images of SnO₂–B₂O₃ composites as a function of B₂O₃ content: (a) B 0%, (b) B 0.9%, (c) B 1.1%, (d) B 1.9%, (e) B 2.1%, and (f) B 3.2%.

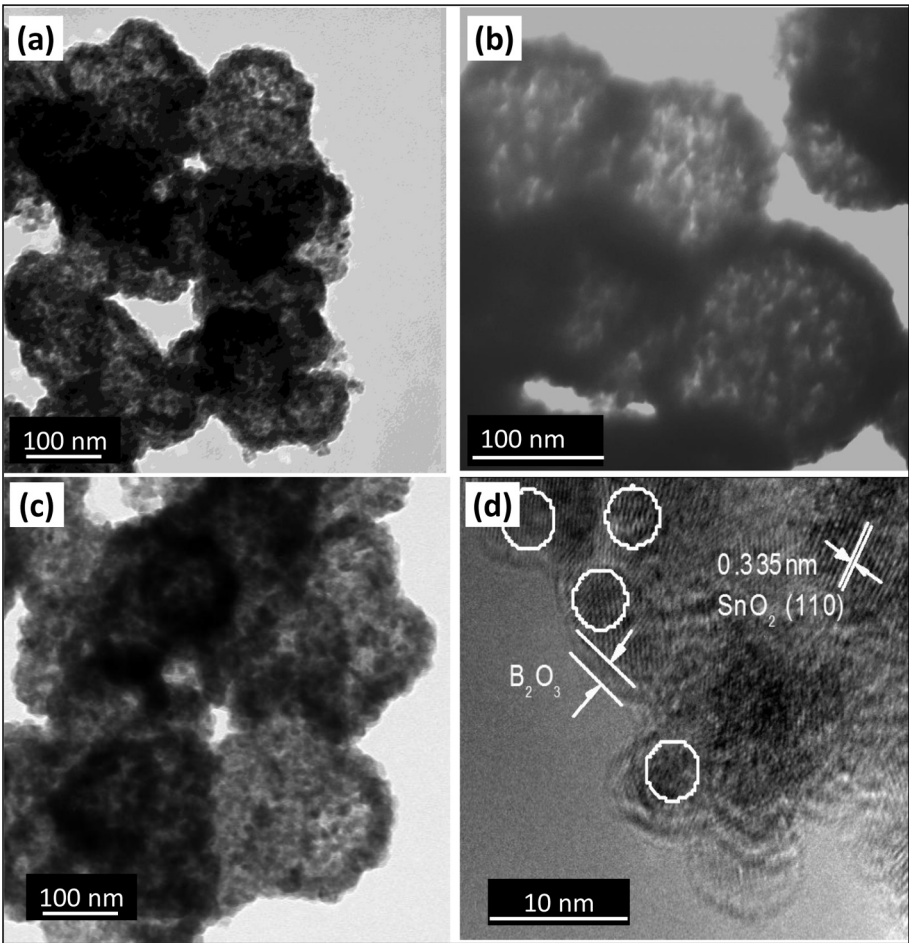


Fig. 4. TEM images for hollow SnO₂ (a, b) and hollow SnO₂–B₂O₃ composites (B 2.1%) (c, d).

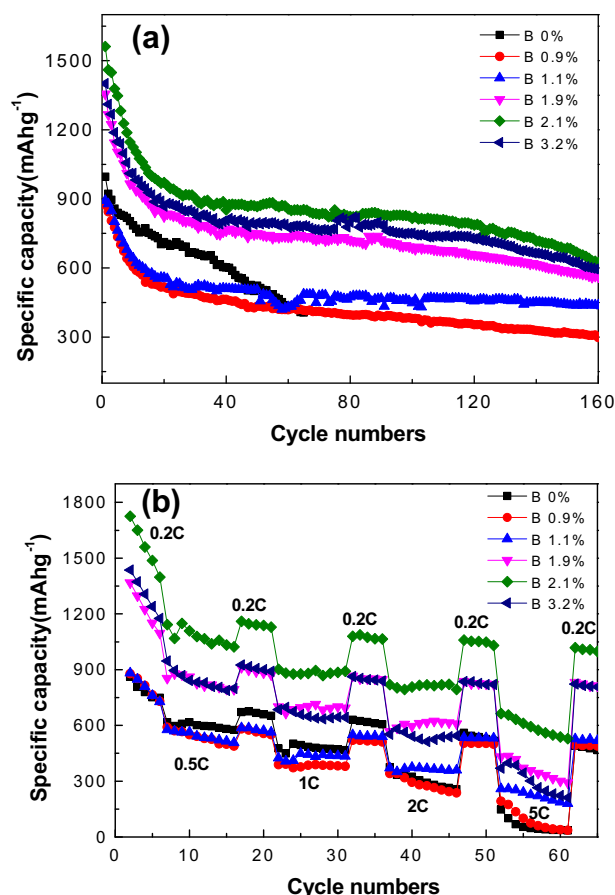


Fig. 5. Cycling performance (a) and rate capability (b) for the hollow SnO₂–B₂O₃ composite anodes as a function of B₂O₃ content.

3.2. Electrochemical performance

Fig. 5a shows comparative discharge–charge cycling performance for different hollow SnO₂–B₂O₃ core–shell composite anodes at a rate of 0.2 C in a voltage window of 0.04–2 V. Except for the hollow SnO₂ anode (B 0%) with low cycles of 65, due to the significant capacity loss, discharge capacity of all of SnO₂–B₂O₃ composite anode was studied as a function of B₂O₃ content up to 160 discharge–charge cycles. In particular, specific capacities of 297.6 mAh g⁻¹ for B 0.9%, 438.6 mAh g⁻¹ for B 1.1%, 561.4 mAh g⁻¹

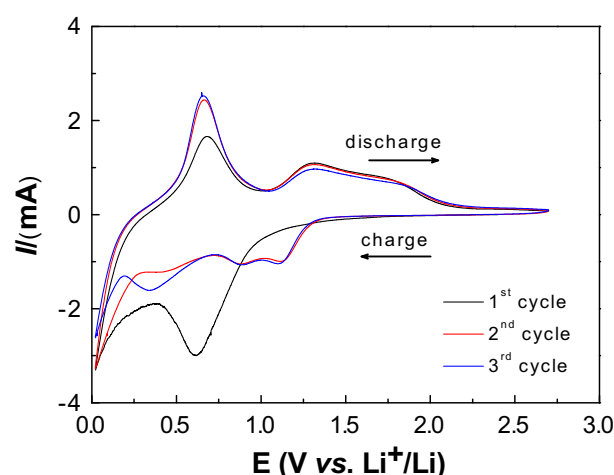


Fig. 7. The CV curves of the B 2.1% electrode during the first three cycles.

for B 1.9%, 622.7 mAh g⁻¹ for B 2.1%, and 593.2 mAh g⁻¹ for B 3.2% were measured. Most recently, high-performance SnO₂ composite anodes were developed for LIBs. For instance, a binder-free SnO₂ electrode was fabricated without using PVDF, showing a discharge capacity of 504 mAh g⁻¹ after the 50th cycle at a rate of 0.1 C [34]. A novel SnO₂/graphene composite consisting of SnO₂ nanoparticles confined in a graphene framework exhibits a capacity of 521 mAh g⁻¹ after 50 cycles at a current density of 100 mA g⁻¹ [35]. In addition, a SnO₂/mesoporous starburst carbon composite anode is able to retain a capacity of about 1100 mAh g⁻¹ during the 30th cycle at the current density of 80 mA g⁻¹ [36]. In this work, the best performing hollow SnO₂–B₂O₃ core–shell composite retains specific capacity of 622.7 mAh g⁻¹ after 160 cycles at a current density of 156 mA g⁻¹, demonstrating improved or comparable performance when compared to these reported SnO₂ anodes to date [8,31–36]. A promotional role of B₂O₃ is clearly observed with the SnO₂–B₂O₃ composite anodes. In the hollow SnO₂–B₂O₃ core–shell composite, hollow SnO₂ space is able to mitigate the enormous volume changes. More importantly, the much improved cycle stability can be attributed to the addition of inactive B₂O₃ buffer layers [37], accommodating the enormous volume changes during lithium insertion/extraction processes and keeping the SnO₂ particles from agglomeration during the cycling. In addition, a synergistic effect between the hollow structure [5,22,31] and the inactive B₂O₃ buffer layer [25] is also likely, which can reduce the overall volume expansion more effectively. Noteworthy, the discharge capacity measured with the SnO₂–B₂O₃ composite anodes are larger

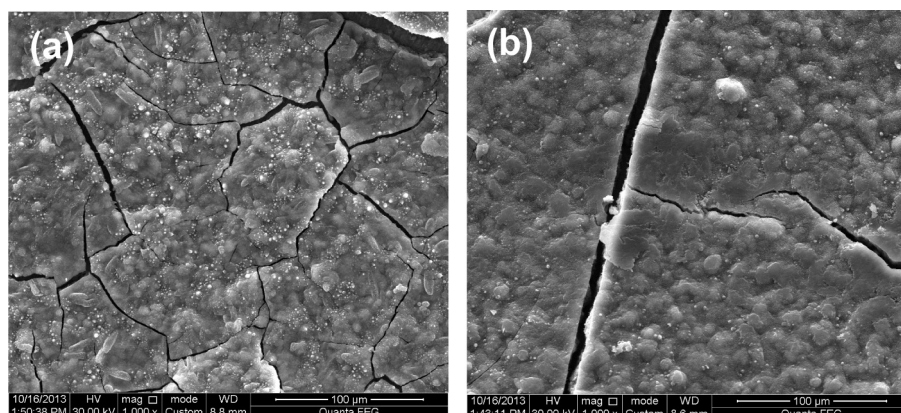
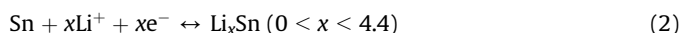


Fig. 6. SEM images of the cycled electrodes: (a) B 0% after 70 cycles, and (b) B 2.1% after 160 cycles.

than the theoretical reversible capacity of SnO_2 (780 mAh g^{-1}) in many cycles. Apart from the partially reversible reaction as described in Eq. (1), the hollow structure is able to provide more interfacial area for de-embedding lithium [21,22]. Also, B_2O_3 itself shows almost no lithium storage capacity, however the increased storage capacity can be attributed to the modification of the electronic structure of the host materials after the introduction of boron oxide, and thus more lithium species are reversibly inserted into the host matrix [30,38]. From Fig. 5(a), it can be seen that cycling performance degradation occurs rapidly during the first 20 cycles. Alloying/dealloying mechanism of Li_xSn associated with Li intercalation/de-intercalation was proposed [7].



Although the lithia matrix formed during the initial stages helps hold the Li–Sn regions together through the large volume changes

in the alloying/dealloying process, the calculated volume per mole of Sn atoms in each of the Li–Sn phases is colossal compared to metallic Sn. Especially, the large volume increase factor to the alloying limit of $\text{Li}_{22}\text{Sn}_5$ is 3.59. The huge volume expansion of SnO_2 electrodes during the charge–discharge process probably leads to the crack, pulverization and consequent rapid cycle degradation during initial cycles.

The charge–discharge rate performance of the hollow SnO_2 – B_2O_3 core–shell composites was studied by increasing rates from 0.2 C (156 mA g^{-1}) to 5 C (3900 mA g^{-1}) as shown in Fig. 5(b). As for each high rate stage, the cell was cycled for 10 times. Between any two high rates, the discharge–charge current is reduced to 0.2 C for 5 cycles. The specific capacity of the composites is superior to that of SnO_2 microspheres at all charge/discharge rates. The B 2.1% anode (around 20 wt% B_2O_3) exhibited the best rate performance. For instance, at a rate of 5 C, the specific capacity of B 2.1% is above 528.6 mAh g^{-1} , which is much greater than that of any other samples. When the rate was reduced to 0.2 C, the discharge capacities were recovered to about 1000 mAh g^{-1} , indicating high capacity retention associated with the excellent structural stability. Thus, the newly prepared hollow SnO_2 – B_2O_3 core–shell composite anodes demonstrated significantly improved rate performance, compared to any other SnO_2 anodes [15,16,19,21]. This enhancement is ascribed to boron atoms which may act as an electron-acceptor during the electron transfer process accompanied with lithium insertion due to the electron-deficient nature of boron [24]. Another reason is that a boron ion occupies the interstitial site and releases three free electrons, resulting in an increase of free electron density [39]. Nonetheless, an excessive B_2O_3 content leads to a decrease in performance, due to a poor electronic conductivity of B_2O_3 . Thus, the ideal balance between the enhanced electron-acceptor effect and the compromised electronic conductivity yields an optimal B_2O_3 content around 20 wt%. These results confirm that the incorporation of a B_2O_3 coating is an effective solution to enhance SnO_2 anode performance.

The morphology of SnO_2 and SnO_2 – B_2O_3 composite electrodes after cycling was studied using SEM images, as shown in Fig. 6. Enormous volume change during the charge–discharge process was observed with the SnO_2 electrode. After 70 charge–discharge cycles, significant cracks appear on the SnO_2 electrode (Fig. 6a) due to the large volume expansion and phase transition, thereby leading to the loss of electrical contact between the active materials and the current collector. Compared to the SnO_2 electrode, the SnO_2 – B_2O_3 composite electrode shows much less cracks even after 160 cycles (Fig. 6b). The result further indicates that the B_2O_3 coating onto SnO_2 is able to relieve the large volume expansion to some extent. Consequently, the cyclic stability of SnO_2 – B_2O_3 composites electrode is greatly improved relative to SnO_2 , due to the presence of B_2O_3 coating.

According to above examined data, it is noted that the B 2.1% electrode (SnO_2 – B_2O_3 with 20 wt% B_2O_3) exhibits the best cycling performance and rate capabilities. The improved cycle stability and rate capabilities motivate us to further investigate the effect of B_2O_3 on electrochemical activity of SnO_2 . Fig. 7 shows the CV curves of B 2.1% electrode for the first three cycles in the potential range of

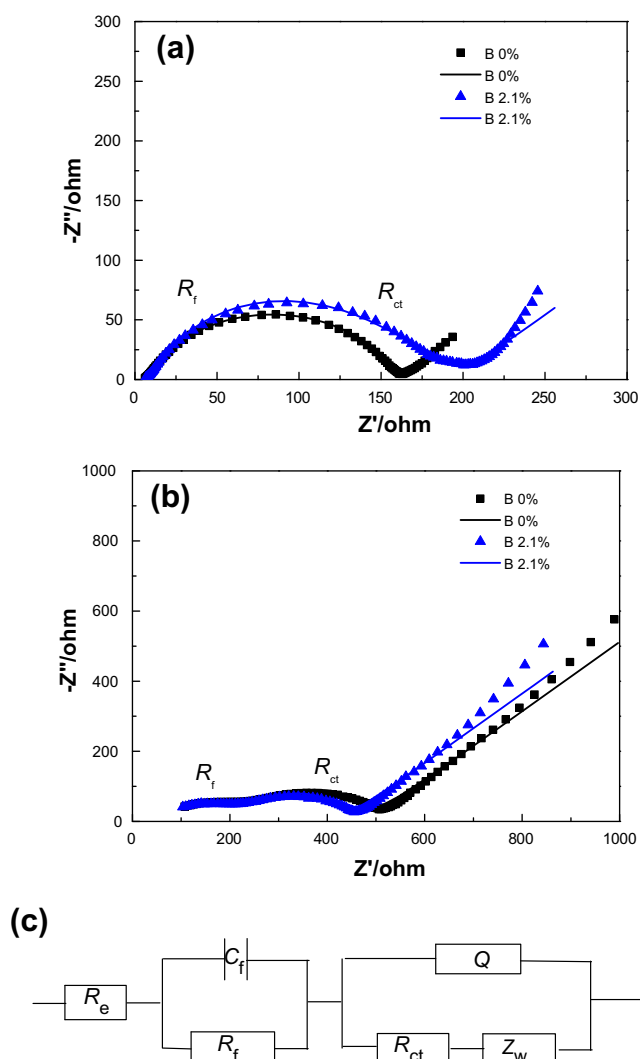


Fig. 8. EIS for both B 0% and B 2.1% electrodes after the 4th charge–discharge cycle (a) and the 30th cycle (b). Symbols represent experimental spectra and continuous lines represent fitted data using the equivalent electrical circuit shown in (c). R_e – electrolyte ohmic resistance, R_f – resistance for Li^+ migration through the passivation film, C_f – constant phase element (CPE), R_{ct} – passivation film capacitance, Z_w – finite length Warburg impedance, R_{ct} – charge transfer resistance, R – total resistance.

Table 2

Simulated parameters of the elements on equivalent circuits for the lithium insertion reaction on B 0% (B_2O_3 free) and B 2.1% (SnO_2 – B_2O_3) anodes at different cycles.

Samples	$R_e/[\Omega]$	$R_f/[\Omega]$	$R_{ct}/[\Omega]$	$R/[\Omega]$
B 0% (4th)	6.1	1.6	151.1	158.8
B 2.1% (4th)	5.9	78.9	112.9	197.7
B 0% (30th)	14.9	106.2	376	497.1
B 2.1% (30th)	14.3	100.9	326.3	441.5

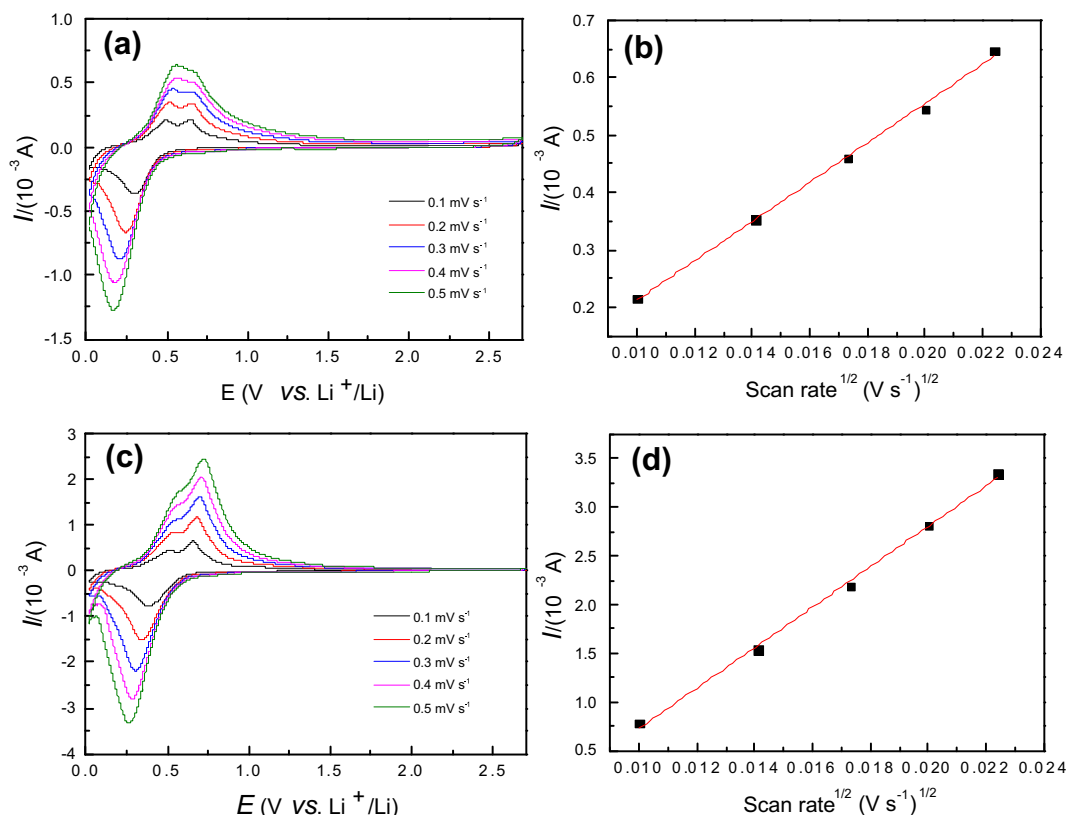


Fig. 9. Cyclic voltammograms of (a) B 0% and (c) B 2.1% electrodes. The scan rates are 0.1, 0.2, 0.3, 0.4 and 0.5 mV s^{-1} . Plot of peak current (I_p) as a function of the square root of the scan rates ($v^{1/2}$) for B 0% (b) and B 2.1% electrodes (d).

0.02–2.70 V at a scan rate of 0.5 mV s^{-1} so as to analyze the lithium ions insertion–extraction process in the hollow $\text{SnO}_2\text{--B}_2\text{O}_3$ core–shell composites. The CV curves of B 2.1% are in good agreement with the characteristic of SnO_2 microspheres reported previously [5]. Thus, the addition of B_2O_3 has no influence on the lithium insertion–extraction reactions of SnO_2 . As described in Eq. (1), during the first cathodic scan, the peak at 0.61 V is ascribed to the reduction of SnO_2 to Sn. The formation of Li_2O or solid electrolyte interface (SEI) layers [23] is responsible for the irreversible capacity loss during the initial cycles. The cathodic peak at 0.02 V and the anodic peak at 0.68 V are assigned to the alloying and dealloying of Li_xSn , respectively [7], as described in Eq. (2). Additionally, an oxidation peak around 1.3 V and a reduction peak around 1.1 V are also observed, which are most likely due to the partially reversible formation/decomposition of Li_2O [1,40]. This partially reversible reaction may further enhance the overall Li storage capacity in SnO_2 anodes [23,31]. The CV profiles after the first cycle almost overlap, in support of the good reversibility of the electrochemical reaction in SnO_2 anodes [41].

In order to further understand the underlying mechanisms for the much improved cycle stability and rate capability resulting from the addition of B_2O_3 , EIS measurements for B 0% (without B_2O_3) and B 2.1% electrodes (around 20 wt% B_2O_3) were performed at 0.4 V during the 4th (Fig. 8a) and 30th (Fig. 8b) charge–discharge cycles. As shown in Fig. 8a, Nyquist plots of both B 0% and B 2.1% electrodes consist of a semicircle and a straight line, referring to the overall resistance at interface and the diffusion of Li^+ in the bulk electrode, respectively. A possible equivalent circuit similar to those previously reported [42–45] is given in Fig. 8c and was used to stimulate the experimental spectra. In Fig. 8a, there are no obvious two semicircles corresponding to the resistance for Li^+ migration

through the passivation film (R_f) and the charge transfer resistance (R_{ct}), probably because the semicircle is a combination of these two elements. However, using the equivalent circuit, the values for R_e , R_f , R_{ct} , and R simulated from EIS data were listed in Table 2. It can be seen the value of R_f of B 2.1% (78.9 Ω) is larger than that of B 0% (1.6 Ω). This phenomenon suggested that the passivation film on anode is not only SEI film, but also B_2O_3 film. It also provided indirect evidence of B_2O_3 coating covering onto the hollow SnO_2 microspheres. Meanwhile, R_{ct} values for B 0% and B 2.1% are 151.1 and 112.9 Ω , respectively. The decreased charge transfer resistance indicates the enhanced ionic conductivity in the composite because of the presence of B_2O_3 , which is beneficial for Li^+ insertion/extraction into the anodes. Regarding the total resistance, the stimulated results indicate that the value of B 0% ($\sim 160 \Omega$) is lower than B 2.1% ($\sim 200 \Omega$). This means that B 2.1% electrode has excellent rate performances, but shows a high resistance. It looks like that the results of impedance and rate performance are not in good agreement. The possible reasons are discussed at here. Although the increasing B_2O_3 content lead to an increase of total resistance due to the poor electronic conductivity of B_2O_3 , the boron atom may act as an electron-acceptor to accelerate charge transfer during the lithium insertion thanks to the electron-deficient nature of boron. In addition, boron ion can occupy the interstitial site and release three free electrons, resulting in an increase of free electron density [24,39]. Overall, the positive effect of B_2O_3 on ionic conductivity of $\text{SnO}_2\text{--B}_2\text{O}_3$ nanocomposites is dominant compared to its negative effect of increasing electrical resistance, thereby improving the rate performance.

The profiles of semicircles in Nyquist plots change with charge–discharge cycles. Especially, after 30th cycle (Fig. 8b), two semicircles become more obvious. According to the simulated

parameters listed in Table 2, the R_f and R_{ct} values increase after 30 cycle for both B 0% and B 2.1% electrodes. These values are comparable with those of other reported oxide anode and cathode materials [45–47]. The increase of R_{ct} with the increasing cycle number is likely due to the reduction of reaction active sites and possible cracks and pulverization of electrode during the Li^+ insertion/extraction reactions. Also, the formation of new SEI film on newly exposed electrode surface leads to an increase of R_f value. Importantly, both R_{ct} and R_f values of B 2.1% electrode become smaller than those of B 0% electrode after 30th charge cycle. The possible reason is that the B 0% electrode has more cracks, which could lead to the loss of electrical contact between the active materials and the current collector. These results further indicate that the incorporation of B_2O_3 coating is an effective method for mitigating volume expansion of hollow SnO_2 microspheres and maintaining good electron transport.

In order to elucidate the excellent rate capabilities of $\text{SnO}_2\text{--B}_2\text{O}_3$ composite anodes, the diffusion coefficient of Li^+ ions (D_{Li}) for both SnO_2 and $\text{SnO}_2\text{--B}_2\text{O}_3$ were calculated by using CVs. In particular, the kinetic response is examined to determine the dependence of peak currents (I_p) on scan rates (v). In Fig. 9a and c, the CVs of B 0% and B 2.1% electrodes at different sweep rates (0.1, 0.2, 0.3, 0.4 and 0.5 mV s^{-1}) are compared. The D_{Li} can be calculated from a linear relationship between I_p and $v^{1/2}$ according to the Randles–Sevcik equation [48]:

$$I_p = 2.69 \times 10^5 n^{3/2} A D_{\text{Li}}^{1/2} C_{\text{Li}}^* v^{1/2} \quad (3)$$

where n is the number of electrons per reaction species (it is 1 for Li^+), A is the electrode area (cm^2), and C_{Li}^* is the bulk concentration of the Li^+ ion in the electrode (mol cm^{-3}). Good linear relationship between I_p and $v^{1/2}$ for both electrodes are demonstrated in Fig. 9b and d, respectively. The Li^+ diffusion coefficient in the B 2.1% electrode is calculated to be $4.5279 \times 10^{-8} \text{ cm}^2 \text{ s}^{-1}$, one magnitude higher than that of calculated for the B 0% electrode ($1.2314 \times 10^{-9} \text{ cm}^2 \text{ s}^{-1}$). The significant enhancement of D_{Li} could be attributed to the B_2O_3 coating, enhancing ionic conductivity in the composite. A higher Li^+ diffusion coefficient is linked to the enhancement of rate capability. Thus, these results also attest the promotional role of B_2O_3 in enhancing the electrochemical performance of hollow SnO_2 anodes for Li-ion batteries.

4. Conclusions

Hollow $\text{SnO}_2\text{--B}_2\text{O}_3$ core–shell composite anodes have been synthesized via a hydrothermal-impregnation method and exhibit enhanced cycling performance and rate capability as compared to pristine hollow SnO_2 microspheres and solid particles $\text{SnO}_2\text{--B}_2\text{O}_3$ composites. This excellent performance can be attributed to the synergistic effect between the hollow SnO_2 structures and the B_2O_3 buffer layers, which accommodates the enormous volume change associated with lithium insertion, and effectively keeps the SnO_2 particles from agglomeration during the charge–discharge process. Ideal loadings of B_2O_3 were found to be approximately 20 wt%. The decreased R_{ct} and much enhanced Li^+ diffusion coefficient due to the presence of B_2O_3 lead to overall high ionic conductivity. All these advantages are beneficial for Li^+ insertion/extraction into the $\text{SnO}_2\text{--B}_2\text{O}_3$ core–shell composite anodes for lithium-ion batteries, showing improved rate performance and cyclic stability.

Acknowledgments

Financial support from the Los Alamos National Laboratory Early Career Laboratory-Directed Research and Development (LDRD) Program (20110483ER) for this work is gratefully acknowledged.

References

- [1] Y. Idota, T. Kubota, A. Matsufuji, Y. Maekawa, T. Miyasaka, *Science* 276 (1997) 1395.
- [2] Y.L. Zhang, Y. Liu, M.L. Liu, *Chem. Mater.* 18 (2006) 4643.
- [3] J. Liu, D.F. Xue, *Electrochim. Acta* 56 (2010) 243.
- [4] D.N. Lei, M. Zhang, Q.Y. Hao, L.B. Chen, Q.H. Li, E.D. Zhang, T.H. Wang, *Mater. Lett.* 65 (2011) 1154.
- [5] R.Q. Liu, N. Li, D.Y. Li, G.F. Xia, Y.M. Zhu, S.Y. Yu, C. Wang, *Mater. Lett.* 73 (2012) 1.
- [6] R.Q. Liu, N. Li, G.F. Xia, D.Y. Li, C. Wang, N. Xiao, D. Tian, G. Wu, *Mater. Lett.* 93 (2013) 243.
- [7] I.A. Courtney, J.R. Dahn, *J. Electrochem. Soc.* 144 (1997) 2045.
- [8] Y. Liang, J. Fan, X.H. Xia, Z.J. Ha, *Mater. Lett.* 61 (2007) 4370.
- [9] Y.N. Nuli, S.L. Zhao, Q.Z. Qin, *J. Power Sources* 114 (2003) 113.
- [10] G.F. Xia, N. Li, D.Y. Li, R.Q. Liu, N. Xiao, D. Tian, *Mater. Lett.* 65 (2011) 3377.
- [11] L.M. Li, X.M. Yin, S. Liu, Y.G. Wang, L.B. Chen, T.H. Wang, *Electrochem. Commun.* 12 (2010) 1383.
- [12] J. Liu, W. Li, A. Manthiram, *Chem. Commun.* 46 (2010) 1437.
- [13] X.W. Lou, C.M. Li, L.A. Archer, *Adv. Mater.* 21 (2009) 2536.
- [14] X.W. Lou, D. Deng, J.Y. Lee, L.A. Archer, *Chem. Mater.* 20 (2008) 6562.
- [15] X.M. Yin, C.C. Li, M. Zhang, Q.Y. Hao, S. Liu, L.B. Chen, T.H. Wang, *J. Phys. Chem. C* 114 (2010) 8084.
- [16] X.W. Lou, Y. Wang, C.L. Yuan, J.Y. Lee, L.A. Archer, *Adv. Mater.* 18 (2006) 2325.
- [17] H.P. Liu, D.H. Long, X.J. Liu, W.M. Qiao, L. Zhan, L.C. Ling, *Electrochim. Acta* 54 (2009) 5782.
- [18] J.L. Cheng, H.L. Xin, H.M. Zheng, B. Wang, *J. Power Sources* 232 (2013) 152.
- [19] G. Wu, N.H. Mack, W. Gao, S. Ma, R. Zhong, J. Han, J.K. Baldwin, P. Zelenay, *ACS Nano* 6 (2012) 9764.
- [20] J. Hassoun, G. Derrien, S. Panero, B. Scrosati, *Adv. Mater.* 20 (2008) 3169.
- [21] X.Y. Zhou, Y.L. Zou, J. Yang, *J. Solid State Chem.* 198 (2013) 231.
- [22] J.S. Chen, Y.L. Cheah, Y.T. Chen, N. Jayaprakash, S. Madhavi, Y.H. Yang, X.W. Lou, *J. Phys. Chem. C* 113 (2009) 20504.
- [23] Y.S. Lin, J.G. Duh, M.H. Hung, *J. Phys. Chem. C* 114 (2010) 13136.
- [24] H.Q. Xiang, S.B. Fang, Y.Y. Jiang, *Solid State Ionics* 148 (2002) 35.
- [25] G.F. Xia, N. Li, D.Y. Li, R.Q. Liu, N. Xiao, D. Tian, *Mater. Lett.* 79 (2012) 58.
- [26] J.D. Mackenzie, W.F. Claussen, *J. Am. Ceram. Soc.* 44 (1961) 79.
- [27] C.H. Hsu, C.J. Huang, *Int. J. Appl. Ceram. Technol.* 10 (5) (2013) 773.
- [28] J. Morales, L. Sánchez, *Solid State Ionics* 126 (1999) 219.
- [29] C.X. Chen, S.P. Wu, Y.X. Fan, *J. Alloys Compd.* 578 (2013) 153.
- [30] X.D. Wu, Z.X. Wang, L.Q. Chen, X.J. Huang, *Solid State Ionics* 170 (2004) 117.
- [31] S.J. Han, B.C. Jang, T. Kim, S.M. Oh, T. Hyeon, *Adv. Funct. Mater.* 15 (2005) 1845.
- [32] J.F. Ye, H.J. Zhang, R. Yang, X.G. Li, L.M. Qi, *Small* 6 (2010) 296.
- [33] L.F. Cui, J. Shen, F.Y. Cheng, Z.L. Tao, J. Chen, *J. Power Sources* 196 (2011) 2195.
- [34] K. Ui, S. Kawamura, N. Kumagai, *Electrochim. Acta* 76 (2012) 383.
- [35] Y.H. Hwang, E.G. Bae, K.S. Sohn, S. Shim, X. Song, M.S. Lah, M. Pyo, *J. Power Sources* 240 (2013) 683.
- [36] J. Chen, K. Yano, *ACS Appl. Mater. Interfaces* 5 (2013) 7682.
- [37] V.A. Mukhanov, O.O. Kurakevich, V.L. Solozhenko, *J. Superhard Mater.* 30 (2008) 71.
- [38] X.D. Wu, Z.X. Wang, L.Q. Chen, X.J. Huang, *J. Electrochem. Soc.* 151 (2004) A2189.
- [39] B. Zhang, Y. Tian, J.X. Zhang, W. Cai, *Vacuum* 85 (2011) 986.
- [40] M. Winter, J.O. Besenhard, M.E. Spahr, P. Novak, *Adv. Mater.* 10 (1998) 725.
- [41] G. Xia, N. Li, D. Li, R. Liu, C. Wang, Q. Li, X. Lu, J.S. Spendlow, J. Zhang, G. Wu, *ACS Appl. Mater. Interfaces* 5 (2013) 8607.
- [42] Z.Y. Chen, C.S. Dai, G. Wu, M. Nelson, X.G. Hu, R.X. Zhang, J.S. Liu, J.C. Xia, *Electrochim. Acta* 55 (2010) 8595.
- [43] C.S. Dai, Z.Y. Chen, H.Z. Jin, X.G. Hu, *J. Power Sources* 195 (2010) 5775.
- [44] C. Wang, D.L. Wang, Q.M. Wang, H.J. Chen, *J. Power Sources* 195 (2010) 7432.
- [45] M.V. Reddy, T. Yu, C.H. Sow, Z.X. Shen, C.T. Lim, G.V. Subba Rao, B.V.R. Chowdari, *Adv. Funct. Mater.* 17 (2007) 2792.
- [46] K.S. Tan, M.V. Reddy, G.V. Subba Rao, B.V.R. Chowdari, *J. Power Sources* 141 (2005) 129.
- [47] M.V. Reddy, S. Madhavi, G.V. Subba Rao, B.V.R. Chowdari, *J. Power Sources* 162 (2006) 1312.
- [48] T. Zhang, L.J. Fu, J. Gao, Y.P. Wu, R. Holze, H.Q. Wu, *J. Power Sources* 174 (2007) 770.